Further Study on a PWM Current-Source-Converter-Based Wind Energy Conversion System Considering the DC-Link Voltage

Qiang Wei, Bin Wu, *Fellow, IEEE*, Dewei Xu, *Member, IEEE*, and Navid R. Zargari, *Fellow, IEEE*

***Abstract*—Previous research on the series-connected pulsewidth modulation current-source-converter-based offshore wind energy conversion system is conducted without considering the effects of the independent control of offshore converters and the cables connected between offshore converters and between offshore and onshore converters. In the present work, a further study on the system is conducted taking these factors into consideration. First, the equivalent circuit of the system is derived, based on which two items are selected to evaluate the performance of the system: the dc-link current and the dc-link voltage. Second, both the dc-link current and the dc-link voltage are derived and analyzed, and the worst case is quantitatively and qualitatively defined. Third, the performance of the system with dc filters is investigated. Finally, both simulation and laboratory-scale experiments are provided.**

***Index Terms*—Current-source converter (CSC), dc filter, dc-link current, dc-link voltage, offshore wind energy conversion systems.**

I. Introduction

OFFSHORE wind power is attracting increasingly attention because of the considerable wind resources, higher and steadier wind speeds, and minimized environmental effects [1]. Apart from considering reliability and efficiency as the main requisites for all onshore systems, footprints and weights are particularly important for offshore systems [2]. Based on the connection methods of wind turbines in offshore wind farms, existing configurations can be mainly classified into two categories. One is the parallel-connected configuration, which is already implemented in practice, such as ABB and SIEMENS [3], [4]. The biggest challenge for this configuration is the very bulky and costly offshore substation required to house all the step-up transformers and converters [4]. The other is the series-connected configuration. By directly connecting the output of

Manuscript received May 18, 2018; accepted August 12, 2018. Date of publication August 19, 2018; date of current version April 20, 2019. Recommended for publication by Associate Editor L. Chang. *(Corresponding author: Qiang Wei.)*

Q. Wei is with the Department of Electrical Engineering, Lakehead University, Thunder Bay, ON P7B 5E1, Canada (e-mail:

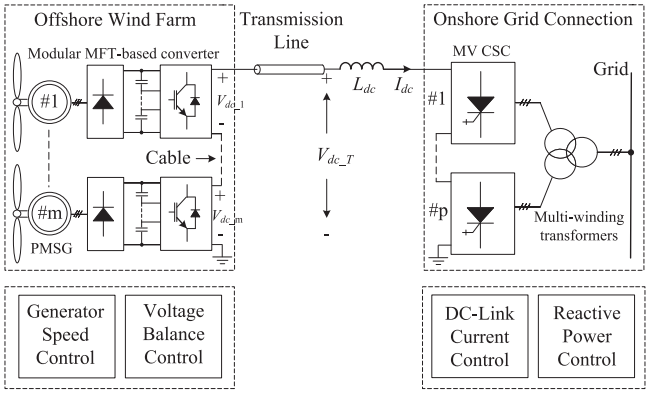

Fig. 1. MFT-based offshore wind farm configuration [14].

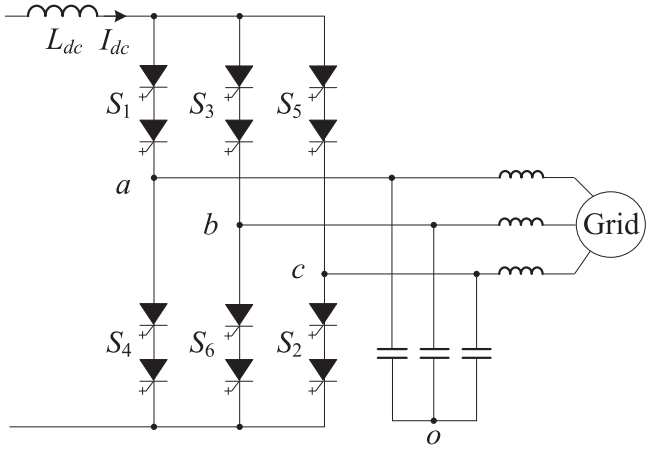

Fig. 2. Current-source converter.

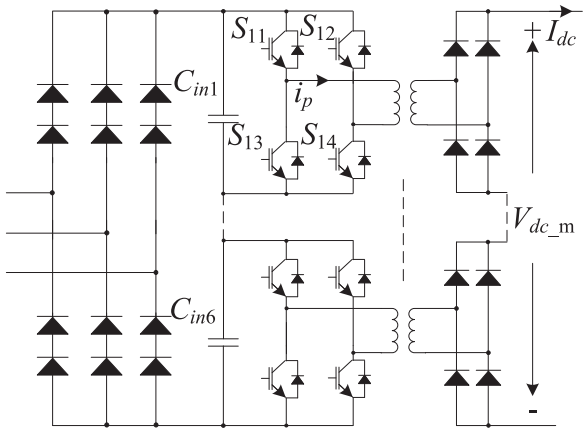

Fig. 3. Modular MFT-based converter.

is the dc-link current used for system control and the other is the dc-link voltage that determines the system insulation level. Second, both the dc-link current and the dc-link voltage are derived and analyzed, and the worst case and its condition are quantitatively and qualitatively defined. Third, a dc filter is introduced to each offshore converter to lower the dc-link voltage and the system with dc filters is analyzed, and a case study on the design of the dc filter and the dc-link inductor of the system is illustrated. In summary, compared with previous works [13]–[17], the main contributions of the present work are the following: the worst case of the dc-link voltage and the dc-link current of the CSC-based system considering the above-mentioned factors is investigated and defined, and a solution is given.

II. CSC-Based Wind Energy Conversion System

Fig. 1 shows the recently proposed MFT-based configuration for the series-connected CSC-based offshore wind farm [14]. In the offshore wind farm, a number of MV turbine units are connected in series to reach an HVdc level. The permanent magnet synchronous generator (PMSG) with low cost of maintenance is employed. The generator-interfaced converter consists of a low-cost and robust passive rectifier and a modular MFT-based converter. In the onshore station, a number of MV CSCs are connected to form a centralized dc–ac converter connected to the grid through multiwinding transformers. The transformers, here, are to provide galvanic isolation and voltage step-up if required. The dc-link inductor $L_{\rm dc}$ is used to smooth the dc-link current. Generally, there are two control objectives: one is independent offshore converter control including maximum power point tracking, generator speed control, and voltage balance control of the modular MFT-based converter, and the other is onshore control consisting of dc-link current control and reactive power control. The control of offshore and onshore converters is decoupled. See [14] for more details.

Fig. 2 shows the topology of a traditional CSC [18], and Fig. 3 shows the topology of the modular MFT-based converter [14]. The modular MFT-based converter plays two roles. First, it is for generator control. The primary objective for the generator-side converter is to obtain the maximum power input from varying wind speeds, which can be achieved by regulating the modular converter. Second, it is used for galvanic isolation. In a series-connected configuration, the wind generator that is farthest from the grounding must be capable of withstanding the full transmission level, which is impractical for generator, while the MFT helps solve this issue. An MFT is smaller in size and weight than a low-frequency transformer, and this is particularly important for offshore applications as the space either in the nacelle or in the tower is limited. Furthermore, a modular design of the MFT helps reduce the burden of manufacturing as one transformer carries only one part of a megawatt-level power. The modular design of the converter also contributes to the choice of low-cost low-voltage switching devices instead of high-voltage ones.

III. System Investigation Considering Cables

Compared with previous works [13]–[17], two items are selected to evaluate the performance of the system considering the effects of independent control of offshore converter and the cables connected between offshore converters and between offshore and onshore converters: one is the dc-link current used for system control, and the other is the dc-link voltage used for system-insulation-level determination.

A. Equivalent Circuit of Offshore Converters

Fig. 4 shows the key waveforms of one offshore MFT-based converter, where conventional phase-shifted modulation is used.

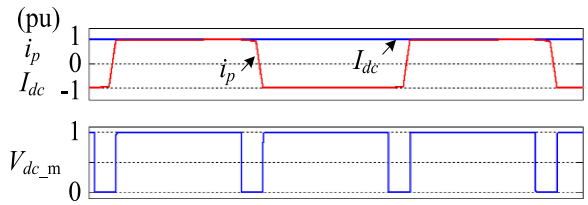

Fig. 4. Output voltage of the MFT-based converter #*m*.

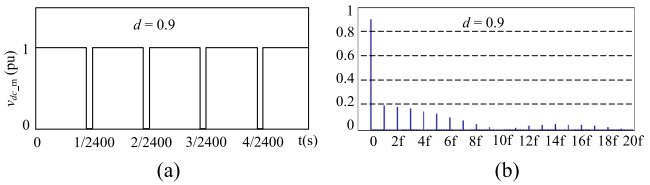

Fig. 5. Pulse-wave voltage source. (a) Time domain. (b) Frequency domain.

As shown in Fig. 4, the output voltage of each offshore converter $v_{\mathrm{dc\_m}}$ is a pulse wave [14].

Therefore, each offshore turbine unit can be replaced with a voltage source driven by a pulse wave $v_{\mathrm{dc\_m}}$, as illustrated in Fig. 4. In practice, to achieve maximum power point tracking, different generator speeds are needed upon different wind speeds, thus generating different terminal voltages of the generators and different magnitudes of $v_{\mathrm{dc\_m}}$ as well. Second, in the series-connected CSC-based configuration, the dc-link current is flowing through all the converters. The one with lower wind speed generates lower power and lower torque/current of the generator, so the resultant duty cycle of the offshore MFT-based converter is smaller. Third, each offshore converter is controlled independently, giving different initial phase angles of $v_{\mathrm{dc\_1}}$ (unit #1) and $v_{\mathrm{dc\_m}}$ (unit #*m*). Therefore, $v_{\mathrm{dc\_1}}$ (unit #1) and $v_{\mathrm{dc\_m}}$ (unit #*m*) cannot be guaranteed to be identical in terms of magnitude, initial phase angle, and duty cycle because of the possibly different wind speeds and independent converter control [14].

Then, the Fourier series equation of the output voltage of each offshore converter $v_{\mathrm{dc\_m}}$ in per unit is expressed as

$$v_{\mathrm{dc\_m}}(t) = d_m + a_{m\_n} \sum_{n=1}^{\infty} \cos\{2\pi n f(t + \Delta t_m)\} \quad (1)$$

where d_m is the duty cycle of $v_{\mathrm{dc\_m}}$ for unit #*m*, a_{m_n} ($0 \leq a_{m\_n} \leq 1$) are magnitude coefficients of the *n*-order component of $v_{\mathrm{dc\_m}}$, and Δt_m represents the initial phase angle of $v_{\mathrm{dc\_m}}$. Note that Δt_m can be any possible numbers, while it can be modified to fall into the range of $0 \leq \Delta t_m \leq 1f$, which corresponds to the period of the fundamental component [14].

For example, the time- and frequency-domain waveforms of $v_{\mathrm{dc\_m}}$ under the rated condition are illustrated in Fig. 5. The duty cycle under the rated condition is around 0.9, and the fundamental frequency (*f*) is 2400 Hz [14].

TABLE I
SIMULATION AND EXPERIMENTAL PARAMETERS

Items	Simulation		Experiment	
	SI	pu	SI	pu
System Rating				
Nominal Power	5 MW	1.0	720 W	1.0
Grid/Load Voltage	4160 V	1.0	120 V	1.0
Rated DC-link Voltage (V_{dc_r})	25 kV	1.0	120 V	1.0
Rated DC-link Current (I_{dc})	200 A	1.0	6 A	1.0
Number of Offshore Converters	5	NA	3	NA
Number of Onshore Converters	5	NA	1	NA
Cables Parameters				
Length of Cable Between Offshore Converters (l_{c_m})	1 km		0 m	
Length of Cable Between Offshore and Onshore Converters (l_{c_r})	50 km		150 m	
Resistance Per Unit Length	0.2 ohms/km		3 ohms/km	
Inductance Per Unit Length	1.4 mH/km		0.15 mH/km	
Capacitance Per Unit Length	0.142 μF/km		0.12 μF/km	
DC Filter and DC-link Inductor				
DC-link Inductor (L_{dc})	175 mH	0.65 pu	30 mH	0.68 pu
DC Filter_Inductor (L_{dc_m})	6 mH	0.13 pu	5 mH	1.1 pu
DC Filter_Capacitor (C_{dc_m})	50 μF	0.32 pu	60 μF	0.4 pu

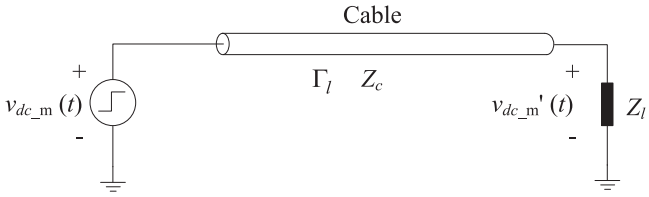

Fig. 6. Configuration of a cable.

B. Equivalent Circuit of Cables

As shown in Fig. 1, single-core submarine cables are used between series-connected offshore converters and between offshore and onshore converters. The key parameters of the cables, such as the length, the capacity, the insulation level, and other parameters, such as capacitance, inductance, and resistance, depend on a number of factors: the configuration of the offshore wind farm [19], height of the wind turbine, system rating, dc-link current, and dc-link voltage [20], [21]. Here, in the present work, the length of the cable between two adjacent offshore converters is set to 1 km, while the one between offshore and onshore converters is set to 50 km for example. All the related parameters are listed in Table I.

Fig. 6 shows such a configuration, where Z_l is to emulate the impedance of the load and Z_c is the characteristic impedance of the cable. According to the well-known principle of the transmission line, the typical characteristics of the voltage reflection coefficient are [22] as follows.

1) If $Z_l = \infty$ (open circuit), $\Gamma_l = 1$, which means the peak value at the end of the cable will be doubled.
2) If $Z_l = 0$ (short circuit), $\Gamma_l = -1$.
3) If $Z_l = Z_c$ (matched impedance), $\Gamma_l = 0$. In this case, there is no voltage reflection in the end of the cable, and the voltages at both ends are same in magnitude.

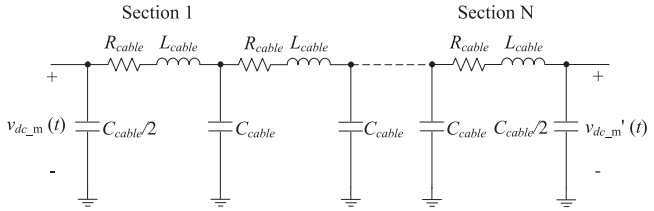

Fig. 7. *RLC*-section-based single-core cable.

From the frequency-domain perspective, the single-core distributed parameter cable can be approximately modeled by cascading a couple of identical *RLC* sections shown in Fig. 7, where the resistance, inductance, and capacitance are uniformly distributed along the cable [22].

An approximation of the maximum frequency range represented by the *RLC* line model is given by the following equation [23]:

$$f_{\max} = \frac{Nv}{8l_c} \tag{2}$$

where *N* is the number of *RLC* sections, l_c is the cable length, and *v* is the propagation speed, that is,

$$v = \frac{1}{\sqrt{L_{\text{cable}} C_{\text{cable}}}}. \tag{3}$$

For example, for a 1-km cable having a propagation speed of around 70 000 km/s [calculated based on (3)], the maximum frequency range represented with a single *RLC* section is approximately 8.75 kHz, while the number for two *RLC* sections is 17.5 kHz. As shown in Fig. 5, the main harmonics are located at below 48 kHz, so a five-*RLC*-section model can be used for well modeling the 1-km cable. Similarly, the 50-km cable connected between offshore and onshore converters needs at least 250 *RLC* sections to represent a frequency of 48 kHz.

Therefore, from the frequency-domain perspective, the voltage at the end of the cable $v'_{\text{dc\_}m}(t)$ shown in Fig. 7 with respect to the one at the beginning of the cable $(v_{\text{dc\_m}})$ can be defined as

$$\begin{aligned} v'_{\text{dc\_}m}(t) &= |H(j2\pi f)|\, v_{\text{dc\_}m}(t) \angle H(j2\pi f) \\ &= H_{m\_n} v_{\text{dc\_}m}(t + \Delta t_m + \Delta t_{c\_m}) \end{aligned} \tag{4}$$

where $|H(j\omega)|$ and $\angle H(j\omega)$ are the gain and phase of the transfer function of the *RLC* section model shown in Fig. 7. For simplicity, $H_{\text{m\_n}}$ is used to represent the gain of the *n*-order component for $v_{\text{dc\_m}}$, Δt_m is defined as same as before, and Δt_{c_m} represents the delay in phase. Note that Δt_{c_m} is proportional to the length of cable (l_{c_m}) given a type of cable, that is,

$$\Delta t_{c\_m} = \frac{l_{c\_m}}{v}. \tag{5}$$

Then, combining (1) and (4) gives the output voltage of each offshore converter considering the effect of cable

$$v'_{\text{dc\_}m}(t) = d_m + H_{m\_n} a_{m\_n} \sum_{n=1}^{\infty} \cos\{2\pi n f(t + \Delta t_m + \Delta t_{c\_m})\}. \tag{6}$$

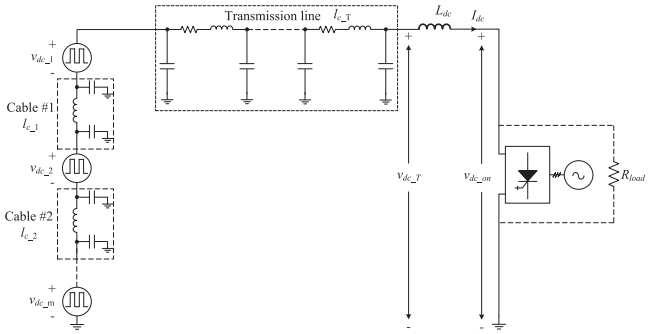

Fig. 8. Equivalent circuit of the system by placing the dc-link inductor onshore.

C. Performance Investigation of the System

Depending on where to place the dc-link inductor, two different equivalent circuits are derived.

1) Case A: DC-Link Inductor Placed at the Onshore Station: The equivalent circuit of the system is shown in Fig. 8. The cables between adjacent offshore converters (l_{c_m}) and between offshore and onshore converters (l_{c_T}) are represented with different numbers of *RLC* sections, as mentioned previously. The onshore grid-connected series-connected CSC is equivalent to a pure resistor R_{load} under the condition of unity power factor. The offshore turbine–generator–converter unit *#m* is replaced with a pulse-wave voltage source, that is, $v_{\text{dc\_m}}$, as mentioned previously.

Compared with conventional studies [22], [23], where the equivalent circuit can be represented as the one shown in Fig. 6, the equivalent circuit derived in the present study is much more complex and has the following two unique features.

1) The offshore converter output voltages [$V_{\text{dc\_1}}(t)$, $V_{\text{dc\_2}}(t)$, ..., $V_{\text{dc\_m}}(t)$ shown in (1)] are pulse-wave voltages and are different in magnitudes, initial phase angles, and duty cycles because of the possible different wind speeds at each turbine and independent control of each offshore converter.
2) Apart from the undersea cable (l_{c_T} shown in Fig. 8) between offshore and onshore converters, the cables (Cable #1, 2, ..., *m*) connected between two adjacent offshore converters must be considered as well, and their effect on the offshore converter output voltages [$V_{\text{dc\_1}}(t)$, $V_{\text{dc\_2}}(t)$, ..., $V_{\text{dc\_m}}(t)$] is illustrated in (6).

Obviously, the equivalent circuit of the present work shown in Fig. 8 is not equivalent to the one in traditional works shown in Fig. 6, and then, the maximum peak value (and its condition) of the voltage at the end of the transmission line ($v_{\text{dc\_}T}$ shown in Fig. 8) of the system shown in Fig. 8 cannot be received just by the well-known principle of the transmission line, as mentioned in Section III-B because the above-mentioned two more factors must be considered. Therefore, how to find the answers considering these factors is worth investigation.

To find the maximum peak value of the dc-link voltage of the system, the equivalent circuit shown in Fig. 8 is simplified, as shown in Fig. 9, with the help of superposition. The impedance

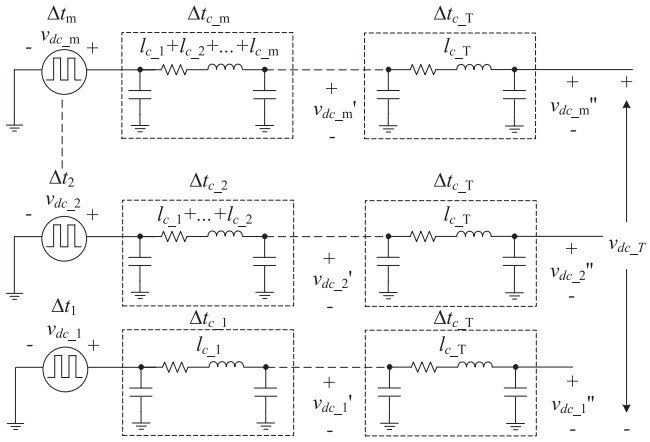

Fig. 9. Simplified equivalent circuit of Fig. 8.

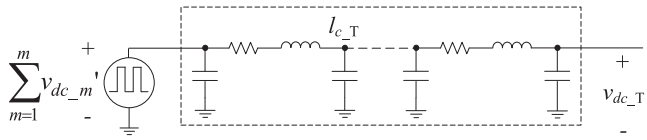

Fig. 10. Further simplified equivalent circuit of the system.

of the dc-link inductor ($L_{\rm dc}$) and the equivalent resistor ($R_{\rm load}$) of the CSCs in series at those frequencies (the fundamental frequency is 2400 Hz) is much larger than that of the cable, which is about 100 Ω; thus, the transmission line can be considered open circuited.

As shown in Fig. 9, the voltage at the end of the transmission line, $v_{\rm dc\_}T$, is expressed as

$$v_{\rm dc\_}T(t) = \sum_{m=1}^{m} v''_{\rm dc\_}m \tag{7}$$

where $v''_{\rm dc\_}m$ is each offshore converter (#m) output voltage at the end of the transmission line. As shown in Fig. 9, the phase angle of $v''_{\rm dc\_}m$ consists of three parts: the initial phase angle of $v_{\rm dc\_m}$ ($\Delta t_{\rm m}$), the phase shift on the cable between offshore converters ($\Delta t_{c\_\rm m}$), and the one on the cable (transmission line) between offshore and onshore converters ($\Delta t_{c\_\rm T}$).

Substituting (6) into (7) yields (8) shown at the bottom of this page.

It is difficult, if not impossible, to calculate the value of (8) in the full operation range, as there are quite a number of uncertain variables. However, only the maximum peak value under the rated condition needs to be considered in practice. Therefore, it is necessary to find the possible maximum peak value of (8) under the rated condition. Under the rated condition, all the wind speeds at turbines are same and maintained at 1 p.u., which means that the magnitudes and duty cycles of all the pulse-wave voltages $v_{\rm dc\_m}$ are same at 1 p.u. The initial phase angles (Δt_m), on the other hand, cannot be guaranteed to be identical because of the independent control of the offshore converter, as analyzed earlier. Besides, the time delay (phase shift) on the cable Δt_{c_m} is known once the cable is fixed, and so does for Δt_{c_T}. And the gain for the n-order ac component H_{m_n} depending on the characteristics of the cable shown in Fig. 7 can also be estimated with the help of MATLAB-based simulation. To sum up, all the variables in (8) can be known or estimated except the initial phase angle Δt_m for $v_{\rm dc\_m}$.

Then, the maximum value of (8) occurs at the condition of

$$\begin{aligned}&(t + \Delta t_1 + \Delta t_{c\_1} + \Delta t_{c\_T})\\ &\quad = (t + \Delta t_2 + \Delta t_{c\_2} + +\Delta t_{c\_T})\\ &\quad = \cdots = (t + \Delta t_m + \Delta t_{c\_m} + \Delta t_{c\_T})\end{aligned} \tag{9}$$

when the voltages at the transmission line $v''_{\rm dc\_}m$ are in phase.

Reorganizing (9) gives

$$(\Delta t_1 + \Delta t_{c\_1}) = (\Delta t_2 + \Delta t_{c\_2}) = \cdots = (\Delta t_m + \Delta t_{c\_m}) \tag{10}$$

which means that when the difference in initial phase angles between $v_{\rm dc\_m}$ and v_{dc_1}, that is, $\Delta t_{\rm m}$–Δt_1, is equal to the difference on the corresponding cables, that is, $\Delta t_{\rm c\_m}$–$\Delta t_{\rm c\_1}$, (8) receives its maximum value. On this basis, the equivalent circuit can be simplified further, as shown in Fig. 10, where $v'_{\rm dc\_}m$ is defined as same as that in Fig. 9.

As shown in Fig. 10, which is same as that in Fig. 6, the maximum peak value of the voltage at the end of the cable $v''_{\rm dc\_}m$ is two times of that of $v_{\rm dc\_m}$ under an open circuit. Therefore, the resultant maximum peak value of the dc-link voltage ($V_{\rm dc\_}T$) is two times of the rated value.

$$\begin{aligned}v_{\rm dc\_}T(t) = &\underbrace{d_1 + H_{1\_n}a_{1\_n}\sum_{n=1}^{\infty}\cos\{2\pi nf(t + \Delta t_1 + \Delta t_{c\_1} + +\Delta t_{c\_T})\}}_{v''_{\rm dc\_1}}\\ &+\underbrace{d_2 + H_{2\_n}a_{2\_n}\sum_{n=1}^{\infty}\cos\{2\pi nf(t + \Delta t_2 + \Delta t_{c\_2} + +\Delta t_{c\_T})\}}_{v''_{\rm dc\_2}}\\ &+\cdots+\underbrace{d_m + H_{m\_n}a_{m\_n}\sum_{n=1}^{\infty}\cos\{2\pi nf(t + \Delta t_m + \Delta t_{c\_m} + +\Delta t_{c\_T})\}}_{v''_{\rm dc\_m}}\end{aligned} \tag{8}$$

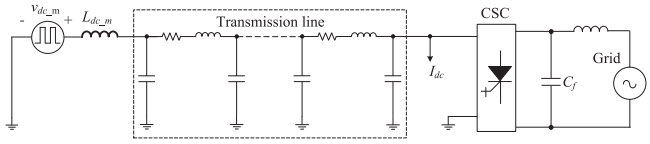

Fig. 11. Equivalent circuit of Case B.

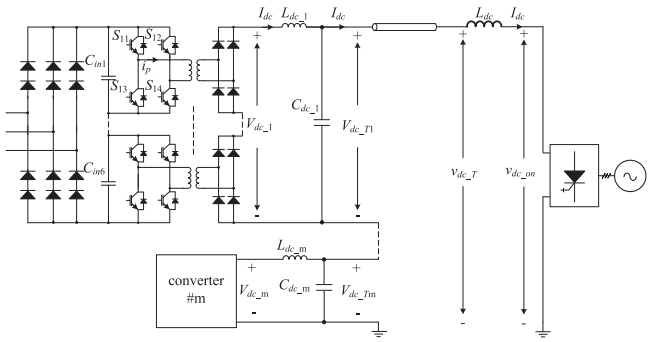

Fig. 12. System with dc filters.

The dc-link current, on the other hand, is not affected. Those ac components of the offshore converter output voltage shown in Fig. 5 produce significantly high inductive reactance on the dc-link inductor. Thus, the resultant ac current in the dc-link current is too small that can be neglected.

To sum up, the maximum peak value of the dc-link voltage when placing the dc-link inductor at the onshore station is two times of the rated value under the condition of (10). The dc-link current is not affected.

2) Case B: DC-Link Inductor Evenly Distributed at Offshore: Another design is evenly placing the dc-link inductor at each offshore converter, that is, $L_{\mathrm{dc\_m}} = L_{\mathrm{dc}}/\mathrm{m}$. However, such a design is not allowed from the circuit perspective. As shown in Fig. 11, the pulse-wave voltage source connected with inductor and the transmission line is equivalent to a voltage source seeing from the onshore CSCs. This equivalent voltage source is then connected in parallel with the capacitor at the output of the CSC, which is not allowed.

D. DC Filter and DC-Link Inductor Design

To avoid the possible two times of the rated value of the dc-link voltage, a dc filter is added to each offshore converter, as shown in Fig. 12. The dc filter helps remove the ac components from the pulse-wave voltage $v_{\mathrm{dc\_m}}$ and keeps its dc component. Then, the problem introduced by the cables is solved. Note that the operation principle of the system with dc filters is different from VSC-based configurations [5]–[9]. In VSC-based configurations, the dc-link voltage should be controlled as a constant under any conditions, and it should also be evenly distributed among the dc-link capacitors. Here, as shown in Fig. 12, the voltage across the capacitors, $V_{\mathrm{dc}\_T\mathrm{m}}$, is decoupled with each other and depends on the varying wind speeds at the turbine. Therefore, there is no voltage-balancing issue among series-connected dc-filter capacitors.

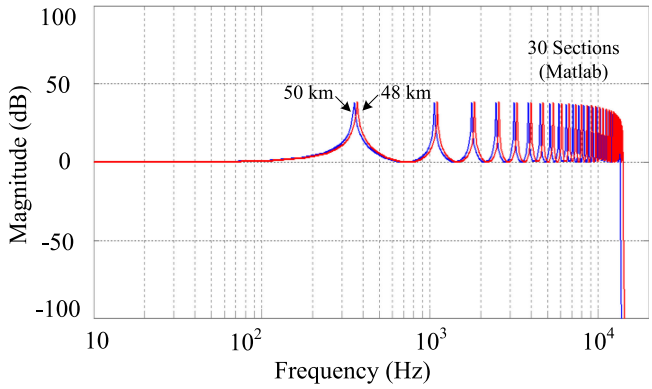

Fig. 13. Magnitude response of the transfer function of the 50-km cable.

The dc-link inductor L_{dc} can be designed by the voltage–second balance principle, that is,

$$(V_{\mathrm{dc\_on}} - V_{\mathrm{dc}\_T}) = L_{\mathrm{dc}} \frac{\Delta I_{\mathrm{dc}}}{\Delta t} \tag{11}$$

where V_{dc_T} is the average dc-link voltage, ΔI_{dc} is the rated dc-link current ripple, $V_{\mathrm{dc\_on}}$ is the voltage across the onshore CSCs, which is clamped by the grid voltage during operation [17], and Δt is the dwell time of the selected vectors of onshore CSCs. Different modulation schemes have different dwell time calculations [24]–[26]. In this work, the typical three-segment sequence is used [24]. Note that because the voltage–second balance principle and the calculation of (11) are mature, they not repeated here.

Similarly, the filter inductor $L_{\mathrm{dc\_m}}$ of each dc filter is

$$(V_{\mathrm{dc}\_m} - V_{\mathrm{dc}\_T\mathrm{m}}) = L_{\mathrm{dc}\_m} \frac{\Delta I_{\mathrm{dc}}}{\Delta t} \tag{12}$$

where $V_{\mathrm{dc}\_T\mathrm{m}} = V_{\mathrm{dc}\_T}/\mathrm{m}$ under the rated condition, Δt is the duty cycle under the rated condition, that is, 0.9 as mentioned earlier, and $V_{\mathrm{dc\_m}}$ and ΔI_{dc} are defined as same as before.

Once the filter inductor $L_{\mathrm{dc\_m}}$ is fixed, the capacitor $C_{\mathrm{dc\_m}}$ can be received based on

$$f_{\mathrm{filter}} = \frac{1}{2\pi\sqrt{L_{\mathrm{dc}\_m} C_{\mathrm{dc}\_m}}}. \tag{13}$$

Note that the cutoff frequency of the dc filter (f_{filter}) is designed based on the worst case, that is, when one of the resonant frequencies of the cable model shown in Fig. 7 is just locating at the fundamental frequency (2400 Hz). For example, for the 50-km cable, the gain for the fundamental component (2400 Hz) is around 40 dB (100 times higher), as shown in Fig. 13. Thus, the attenuation of the dc filter at 2400 Hz should be at least 40 dB (100 times lower) in order to cancel the above possible amplification on the cable. On this basis, the cutoff frequency f_{filter} is selected to be 300 Hz. Note that a smaller attenuation of the dc filter at 2400 Hz, 20 dB (ten times lower), for example, contributes to a smaller filter capacitor, but leads to an increase in the peak value of the dc-link voltage, which is not favorable in practice. In summary, the dc filter parameters are $L_{\mathrm{dc\_m}} = 0.13$ p.u. and $C_{\mathrm{dc\_m}} = 0.32$ p.u., and the dc-link inductor is $L_{\mathrm{dc\_m}} = 0.65$ p.u. under a 15% current ripple.

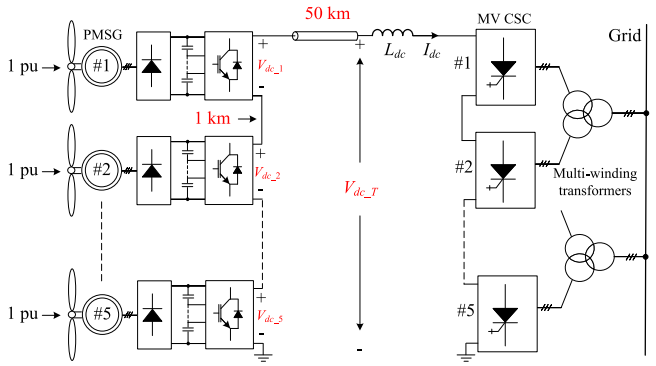

Fig. 14. Diagram of the simulation system.

IV. Simulation and Experimental Investigation

The performance of those control objectives of the system, such as the optimized generator speed control and voltage balance control of the offshore converters, the power balance control, and reactive power control of the onshore converters, and/or the performance of the grid-side current, total harmonic distortion, for example, are affected by the dc-link current rather than the dc-link voltage or the cables and have been thoroughly reported in the previous works [14]–[17], [24], [25], thus not repeated here. Instead, the performance of the dc-link voltage and the dc-link current is the focus.

A. Simulation Investigation

The simulation model is built based on MATLAB/Simulink. The diagram of the simulated system is shown in Fig. 14, where five turbine–generator units and five CSCs are used, and they are operating under the rated condition. As mentioned earlier, the length of the cable between adjacent offshore converters is set to 1 km, and the length of the cable between offshore and onshore converters is 50 km. The control scheme is the same as that reported in previous work [14], thus not repeated here.

Fig. 15 illustrates the simulated performance of the dc-link voltage and dc-link current under the condition of (10). The initial phase angles for $v_{\mathrm{dc\_1}}$, $v_{\mathrm{dc\_2}}$ …, and $v_{\mathrm{dc\_5}}$ are purposely set to 0, Δt_2, Δt_3 …, and Δt_5 to meet the condition of (10). Δt_2 is the time delay on the cable connected between $v_{\mathrm{dc\_1}}$ and $v_{\mathrm{dc\_2}}$, while Δt_5 is the time delay on the cable between $v_{\mathrm{dc\_1}}$ and $v_{\mathrm{dc\_5}}$. As shown in Fig. 15, the peak value of the dc-link voltage is two times of its rated value. The dc-link current, however, is not affected.

Fig. 16 illustrates the simulated performance of the dc-link voltage and the dc-link current without the condition of (10). The initial phase angles for $v_{\mathrm{dc\_1}}$, $v_{\mathrm{dc\_2}}$ …, and $v_{\mathrm{dc\_5}}$ are purposely set to be same, 0, for example. As shown in Fig. 16, the peak value of the dc-link voltage is only 1.6 times of its rated value, which is lower than that in the case of Fig. 15. The dc-link current is not affected. Note that the case shown in Figs. 15 and 16 are only two possible cases of all the possibilities. Fig. 15 shows the worst case, which needs to be considered in practice, while Fig. 16 shows one of other possible cases. It is difficult, if not impossible, to present all the possible cases, since the initial phase angle for each converter voltage $v_{\mathrm{dc\_m}}$ could be any number ranging from 0 to 1/2400 as mentioned earlier, leading to infinite combinations for an m-turbine system.

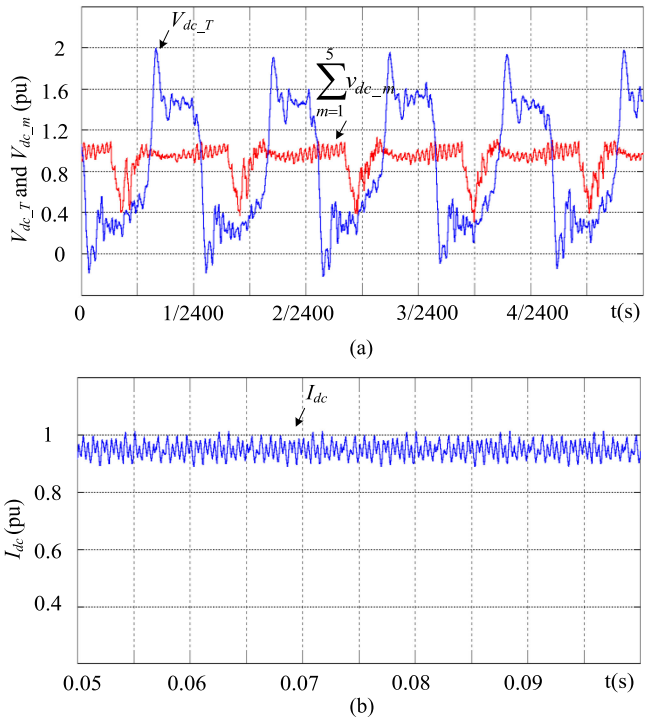

Fig. 15. DC-link voltage and dc-link current under the condition of (10).

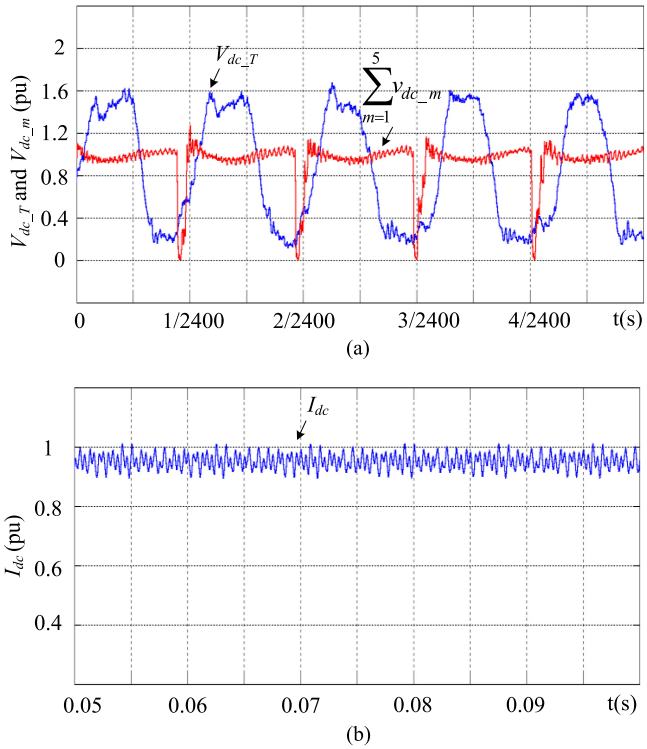

Fig. 16. DC-link voltage and dc-link current without the condition of (10).

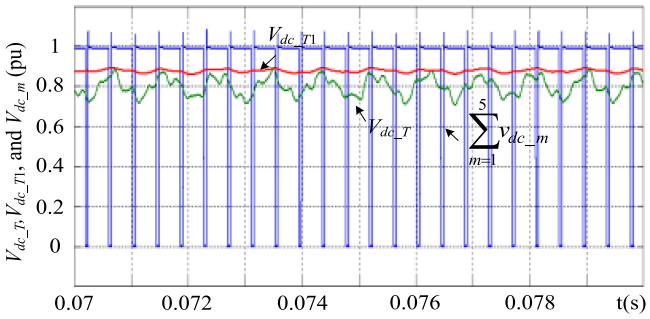

Fig. 17. DC-link voltage with a dc filter (attenuation at 2400 Hz: 40 dB).

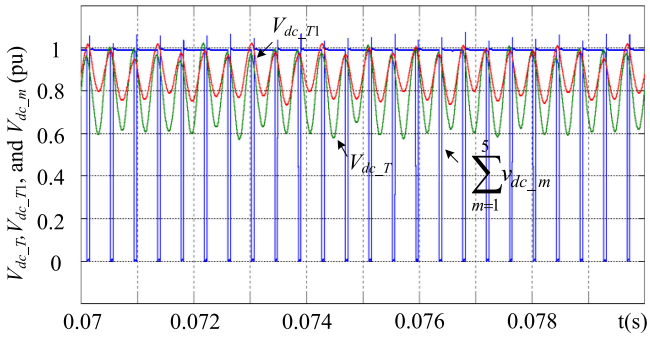

Fig. 18. DC-link voltage with a dc filter (attenuation at 2400 Hz: 20 dB).

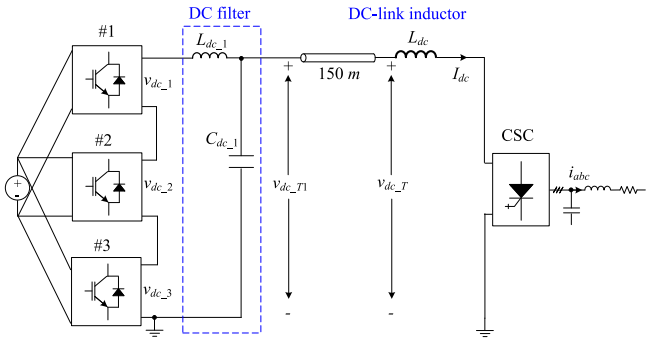

Fig. 19. Experimental circuit.

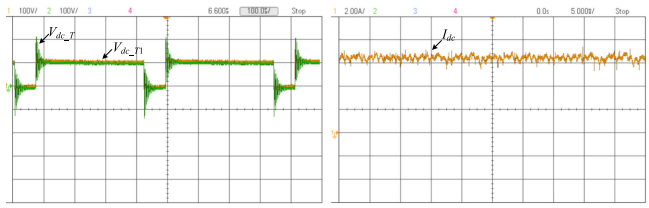

Fig. 20. DC-link voltage before and after the cable without a dc filter.

Fig. 17 shows the dc-link voltage and dc-link current with a dc filter, where the attenuation coefficient at 2400 Hz is 40 dB. The peak value of the dc-link voltage is around 0.44 times of the value without the dc filter, thus giving significant cost saving on system insulation. Fig. 18 shows the dc-link voltage under a different dc filter design, and its attenuation coefficient at 2400 Hz is 20 dB. This dc filter also contributes to lowering the peak value of the dc-link voltage, but with a higher number compared with that in the case of Fig. 17. Obviously, the reduction in the peak value of the dc-link voltage is more preferred due to the significant cost savings on the high-voltage insulated cables rather than on the dc filter capacitor.

B. Experimental Investigation

Laboratory-scale experiments are conducted to investigate the performance of the dc-link voltage and the dc-link current with and without a dc filter. However, two main constraints exist due to the situation of the laboratory-scale setup. One is the length of the cable. The length of the cable used in simulation is 50 km, a minimum value for the HVdc system, which is costly and difficult for layout in the laboratory. In the present work, a 150-m cable is used. The second limit is that the used controller processer cannot achieve the worst-case condition shown in (10) for a 150-m-cable-based setup. The control scheme of the system is processed by dSPACE DS1103, and its minimum fixed step cannot be lower than 20 μs even after simplifying the control scheme. The condition in (10), however, requires a phase shift of 0.2 μs, which cannot be obtained. Therefore, in the present work, the setup is constructed based on the derived equivalent circuit shown in Fig. 10, where the cables between offshore converters are removed. The circuit used for experiments is shown in Fig. 19. The control scheme of the experiment setup consists of two parts. One is the control for the series-connected MFT-based converter, where the traditional phase-shifted modulation is employed. The other is the control of the CSC, where the space-vector modulation is used. As mentioned earlier, the control scheme of the system in the present work is the same as that in the previous work [14] and is thus not repeated here.

Fig. 20 shows the dc-link voltage before and after the 150-m cable and the dc-link current without a dc filter. V_{dc_T1} refers to the voltage at the beginning of the 150-m cable, and V_{dc_T} refers to the voltage at the end of the 150-m cable. The peak value of the dc-link voltage at the end of the cable is two times of that at the beginning of the cable, which verifies that the maximum peak value of the dc-link voltage of the system could be two-times rated. This is the same as that in the simulation. The dc-link current I_{dc}, on the other hand, is not affected mainly due to the high impedance of the dc-link inductor under high frequencies. In contrast with the case in the simulation shown in Figs. 15 and 16, the waveform of the dc-link voltage shown in Fig. 20 is different in shape. This is due to the different lengths of the used cables. In the simulation shown in Figs. 15 and 16, the length of the cable between offshore and onshore converters is 50 km, while it is only 150 m in the experiment. The minimum frequency represented by a 150-m cable is around 250 kHz, as shown in Fig. 21. Thus, only the frequency around 250 kHz could be amplified by the 150-m cable. Fig. 22 shows the fast Fourier transform (FFT) analysis of the dc-link voltages before and after the 150-m cable, where mainly the harmonics around 250 kHz are amplified through the 150-m cable. This can verify the above analysis. To verify the above analysis further, a simulation investigation under a 150-m cable is conducted, as

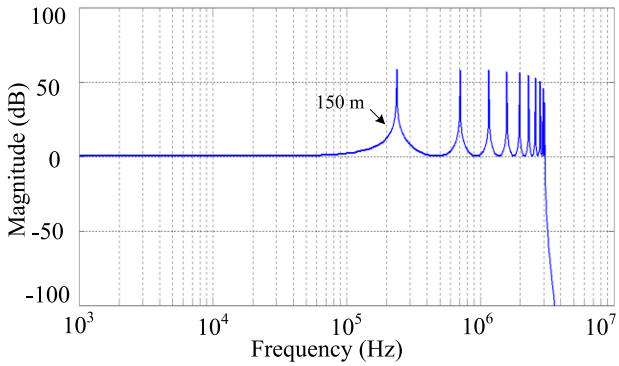

Fig. 21. Magnitude response of the transfer function of the 150-m cable.

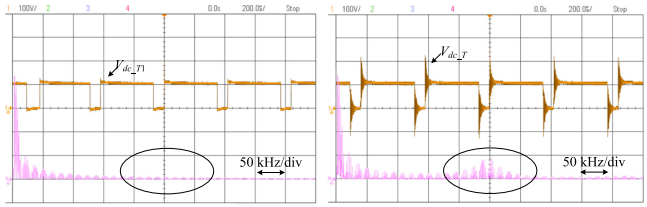

Fig. 22. FFT analysis of the dc-link voltage before and after the cable without a dc filter.

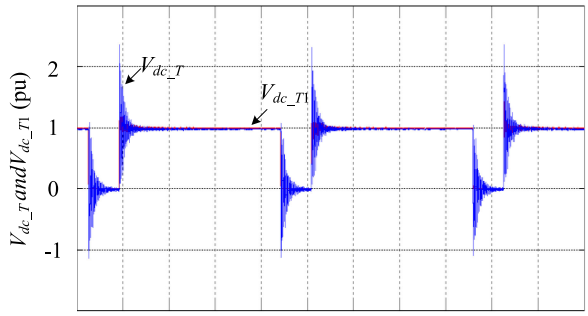

Fig. 23. Simulated dc-link voltage before and after the 150-m cable without a dc filter.

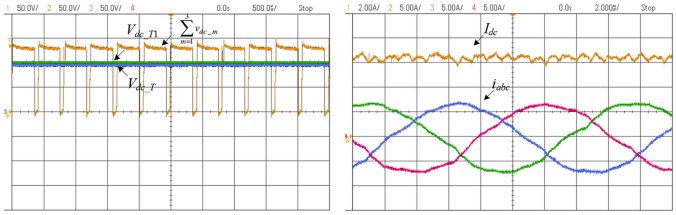

Fig. 24. DC-link voltage and dc-link current with a dc filter.

shown in Fig. 23, where all the parameters are set as same as those in the experiment. As shown in Fig. 23, the peak value of the dc-link voltage at the end of the cable is two times of that at the beginning of the cable, which again verifies that the maximum peak value of the dc-link voltage of the system could be two-times rated.

Fig. 24 shows the waveforms of the dc-link voltage and the dc-link current with a dc filter. The ac components of the dc-link voltage at the beginning of the cable ($V_{\mathrm{dc\_}T1}$) are effectively filtered by the dc filter. As a result, these harmonics disappear at the end of the cable, and thus, the issue of the two-times rated dc-link voltage is well solved. The dc-link current (I_{dc}) is well controlled, and its rated ripple is around 13% under the rated condition. The performance of the load currents (i_{abc}) depends on the used modulation scheme [24]–[26] and is out of the scope of the present work.

V. Conclusion

This work investigates the performance of the PWM CSC-based offshore wind system considering the effects of independent control of offshore converters and the cables connected between offshore converters and between offshore and onshore converters. There are two key findings. First, apart from the cable between offshore and onshore converters, the independent control scheme of offshore converters and the cables between offshore converters affect the maximum peak value of the dc-link voltage. Its maximum peak value occurs when the difference in initial phase angles (time delay) of any two offshore converter output voltages is equal to the difference in the time delay on the corresponding undersea cables (this is different from that in conventional works, where the maximum peak value occurs under only one condition, an infinite load impedance, that is, $Z_l = \infty$). And the maximum peak value is two times of its rated value. Second, the dc-link current is not affected. To solve the issue of higher dc-link voltage, a dc filter is introduced to each offshore converter, and a case study on the design of the dc filter and the dc-link inductor is given.

References

[1] B. Wu, Y. Lang, N. Zargari, and S. Kouro, *Power Conversion and Control of Wind Energy Systems*. New York, NY, USA: Wiley/IEEE Press, 2011.

[2] F. Blaabjerg and K. Ma, "Future on power electronics for wind turbine systems," *IEEE J. Emerg. Sel. Topics Power Electron.*, vol. 1, no. 3, pp. 139–152, Sep. 2013.

[3] Siemens revolutionizes grid connection for offshore wind power plants, 2018. [Online]. Available: http://www.siemens.com/press/pool/de/pressemitteilungen/2015/energymanagement/PR2015100358EMEN.pdf

[4] ABB offshore wind connections, 2018. [Online]. Available: http://new.abb.com/systems/offshore-wind-connections

[5] C. Meyer, M. Hoing, A. Peterson, and R. De Doncker, "Control and design of DC grids for offshore wind farms," *IEEE Trans. Ind. Appl.*, vol. 43, no. 6, pp. 1475–1482, Nov. 2007.

[6] N. Holtsmark, H. J. Bahirat, M. Molinas, B. A. Mork, and H. K. Hoidalen,"An All-DC Offshore wind farm with series-connected turbines an alternative to the classical parallel AC model," *IEEE Trans. Ind. Electron.*, vol. 60, no. 6, pp. 2420–2428, Jun. 2012.

[7] N. Flourentzou, V. Agelidis, and G. Demetriades, "VSC-based HVDC power transmission systems: An overview," *IEEE Trans. Power Electron.*, vol. 24, no. 3, pp. 592–602, Mar. 2009.

[8] S. Lundberg, "Configuration study of large wind parks," *M.S. Thesis*, Chalmers Univ. Technol., Göteborg, Sweden, 2003.

[9] T. H. Nguyen, D. C. Lee, and C. K. Kim, "A Series-connected topology of a diode rectifier and a voltage-source converter for an HVDC transmission system," *IEEE Trans. Power Electron.*, vol. 29, no. 4, pp. 1579–1584, Apr. 2014.

[10] S. Nishikata and F. Tatsuta, "A new interconnecting method for wind turbine/generators in a wind farm and basic performances of the integrated system," *IEEE Trans. Ind. Electron.*, vol. 57, no. 2, pp. 468–475, Feb. 2010.

[11] E. Veilleux and P. Lehn, "Interconnection of direct-drive wind turbines using a series-connected DC grid," *IEEE Trans. Sustain. Energy*, vol. 5, no. 1, pp. 139–147, Jan. 2014.

[12] A. Garcés and M. Molinas, "A study of efficiency in a reduced matrix converter for offshore wind farms," *IEEE Trans. Ind. Electron.*, vol. 59, no. 1, pp. 184–193, Jan. 2012.

[13] M. Popat, B. Wu, F. Liu and N. Zargari, "Coordinated control of cascaded current source converter based offshore wind farms," *IEEE Trans. Sustain. Energy*, vol. 3, no. 3, pp. 557–565, Jul. 2012.
[14] Q. Wei, B. Wu, D. Xu, and N. Zargari, "A medium frequency transformer-based wind energy conversion system used for current source converter based offshore wind farm," *IEEE Trans. Power Electron.*, vol. 32, no. 1, pp. 248–259, Jan. 2017.
[15] Q. Wei, B. Wu, D. Xu, and N. R. Zargari, "Bipolar operation investigation of current source converter-based wind energy conversion systems," *IEEE Trans. Power Electron.*, vol. 33, no. 2, pp. 1294–1302, Feb. 2018.
[16] Q. Wei, B. Wu, D. Xu, and N. R. Zargari, "An optimized strategy for PWM current source converter-based wind conversion system with reduced cost and improved efficiency," *IEEE Trans. Power Electron.*, vol. 33, no. 2, pp. 1202–1210, Feb. 2018.
[17] Q. Wei, B. Wu, D. Xu, and N. R. Zargari, "Power balancing investigation of grid-side series-connected current source inverters in wind energy conversion systems," *IEEE Trans. Ind. Electron.*, vol. 64, no. 12, pp. 9451–9460, Dec. 2017.
[18] B. Wu, *High-Power Converters and AC Drives*. New York, NY, USA: Wiley/IEEE Press, 2006.
[19] A. Kusiak and Z. Song, "Design of wind farm layout for maximum wind energy capture," *Renew. Energy*, vol. 35, no. 3, pp. 685–694, Mar. 2010.
[20] XLPE Submarine Cables, 2018. [Online]. Available: http://new.abb.com/cables
[21] *ABB XLPE Submarine Cable Systems Attachment to XLPE Land Cable Systems, User´s Guide*, ABB, Zürich, Switzerland, 2018.
[22] J. D. Glover, M. S. Sarma and T. J. Overbye, *Power System Analysis and Design*, 5th ed. New Delhi, India: Cengage Learning, 2012.
[23] N. Chaudhuri, B. Chaudhuri, R. Majumder and A. Yazdani, *Multi-terminal Direct-Current Grids: Modeling, Analysis, and Control*. New York, NY, USA: Wiley-IEEE Press, 2014.
[24] Q. Wei, B. Wu, D. Xu, and N. R. Zargari, "A Natural-sampling-based SVM scheme for current source converter with superior low-order harmonics performance," *IEEE Trans. Power Electron.*, vol. 31, no. 9, pp. 6144–6154, Sep. 2016.
[25] Q. Wei, B. Wu, D. Xu, and N. R. Zargari, "Optimal space vector sequence investigation based on natural sampling SVM for medium-voltage current-source converter," *IEEE Trans. Power Electron.*, vol. 32, no. 1, pp. 176–185, Jan. 2017.
[26] X. Guo, D. Xu, and B. Wu, "Common-mode voltage mitigation for back-to-back current-source converter with optimal space-vector modulation," *IEEE Trans. Power Electron.*, vol. 31, no. 1, pp. 688–697, Jan. 2016.

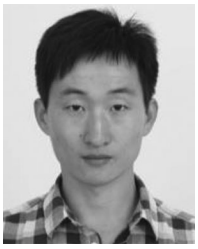

Qiang Wei received the B.Sc. degree from the Henan University of Science and Technology, Luoyang, China, in 2008, the M.A.Sc. degree from Xi'an Jiaotong University, Xi'an, China, in 2012, and the Ph.D. degree from Ryerson University, Toronto, ON, Canada, in 2017, all in electrical engineering.

From 2012 to 2014, he was an R&D Engineer with Delta Power Electronics, Nanjing, China. From 2017 to 2018, he was a Postdoctoral Fellow with Ryerson University. In August 2018, he joined Lakehead University, Thunder Bay, Canada, where he is currently an Assistant Professor. His research interests include renewable energy systems and medium-voltage motor drives.

Bin Wu (S'89–M'92–SM'99–F'08) received the M.A.Sc. and Ph.D. degrees in electrical and computer engineering from the University of Toronto, Toronto, ON, Canada, in 1989 and 1993, respectively.

In 1993, he joined Ryerson University, Toronto, where he is currently a Professor Emeritus. He has authored or coauthored more than 400 technical papers and several Wiley/IEEE Press books. He holds more than 30 granted/pending U.S./European patents in the area of power conversion, medium-voltage drives, and renewable energy systems.

Dr. Wu received the Gold Medal of the Governor General of Canada in 1993, the Premier's Research Excellence Award in 2001, the Natural Sciences and Engineering Research Council Synergy Award for Innovation in 2002, the Ryerson Distinguished Scholar Award in 2003, the Ryerson YSGS Outstanding Contribution to Graduate Education Award, and the Professional Engineers Ontario Engineering Excellence Medal in 2014. He is a Fellow of the Academy of Science of Royal Society of Canada, the Engineering Institute of Canada, and the Canadian Academy of Engineering.

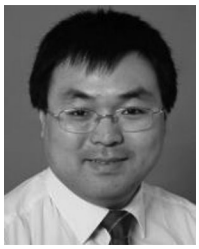

Dewei (David) Xu (S'99–M'01) received the B.Sc., M.A.Sc., and Ph.D. degrees in electrical engineering from Tsinghua University, Beijing, China, in 1996, 1998, and 2001, respectively.

Since 2001, he has been with Ryerson University, Toronto, ON, Canada, where he is currently a Professor. His research interests include renewable energy systems, high-power converters, electric motor drives, and advanced digital control for power electronics.

Navid R. Zargari (M'94–SM'08–F'15) received the B.Eng. degree from the University of Tehran, Tehran, Iran, in 1987, and the M.A.Sc. and Ph.D. degrees from Concordia University, Montreal, QC, Canada, in 1991 and 1995, respectively.

Since 1994, he has been with Rockwell Automation Canada, Cambridge, ON, Canada, first as a Senior Designer, then as the Manager of the Medium Voltage R&D Department, and currently as a Product Architect. For the past 19 years, he has been involved with simulation, analysis, and design of power converters for medium-voltage ac drives. He has coauthored more than 80 research papers and a book entitled *Power Conversion and Control of Wind Energy Systems* (New York, NY, USA: Wiley/IEEE Press, 2011). He holds 30 U.S. granted/pending patents in areas of power converters and medium-voltage applications. His research interests include power converter topologies and their control aspects, power semiconductors, and renewable energy sources.

Dr. Zargari was the recipient of the Premier's Award for the Innovator of the year in 2009 from the Province of Ontario.